Observation of Spin-Induced Ferroelectricity in a Layered van der Waals Antiferromagnet CuCrP$_2$S$_6$

Chang Bae Park, Aga Shahee, Kwang-Tak Kim, Deepak R. Patil, Sergey Alexandrovich Guda, Nikita Ter-Oganessian,* and Kee Hoon Kim*

CuCrP$_2$S$_6$, a van der Waals magnet having stacked layers of 2D honeycomb lattice made of CuS$_3$ triangles and CrS$_6$ octahedra, exhibits an A-type antiferromagnetic order with the Néel temperature (T_N) = 32 K. Upon in-plane magnetic field (H) being applied below T_N, H-induced modulation of the c^*-axis electric polarization (ΔP_{c^*}) is found at fields lower than the saturation field $\mu_0 H_S$ = 6.1 T, at which a forced ferromagnetic alignment sets in. Based on the symmetry analyses and dependence of ΔP_{c^*} on H and the azimuthal angle of applied H direction, a microscopic origin of the magnetoelectric (ME) coupling is attributed to the spin-direction-dependent p–d hybridization that is allowed due to the presence of off-centered Cr^{3+} octahedra. A comparative study on CuCrP$_2$Se$_6$, however, finds no H-induced P modulation due to cancellation of P between neighboring layers with the doubling of a crystallographic unit cell at T_N. As the p–d hybridization mechanism allows generation of P in a single Cr atom–ligand pair, the results imply that large ME coupling should exist even in a single layer limit of CuCrP$_2$S$_6$.

1. Introduction

Coexistence of electric and magnetic orders in multiferroics and their large cross-coupling, i.e., magnetoelectric (ME) coupling, have been intensively investigated to shed light into the

C. B. Park, A. Shahee, K.-T. Kim, D. R. Patil, K. H. Kim
Center for Novel States of Complex Materials Research
Department of Physics and Astronomy
Seoul National University
Seoul 08826, South Korea
E-mail: khkim@phya.snu.ac.kr
S. A. Guda
The Smart Materials Research Institute
Southern Federal University
Rostov-on-Don 344090, Russia
N. Ter-Oganessian
Institute of Physics
Southern Federal University
Rostov-on-Don 344090, Russia
E-mail: teroganesyan@sfedu.ru
K. H. Kim
Institute of Applied Physics
Department of Physics and Astronomy
Seoul National University
Seoul 08826, South Korea

fundamental physics of spin–lattice coupling as well as to uncover potential applications in spintronic devices.[1–4] Various new mechanisms for extracting gigantic ME coupling in single phase as well as artificial composite multiferroics have been proposed and new materials/composite structures are continuously being discovered for nearly two decades.[2,5–7]

Multiferroics should involve spatial inversion and time-reversal symmetry breaking[2] and are categorized into two types (type-I and type-II) based on the origin of electric polarization. Type-I multiferroic materials, having ferroelectricity as a main order parameter, exhibit a conventional ferroelectricity in which asymmetric electronic hybridization is the main source of electric polarization (P), whose magnitude is generally large. However, as the origin of ferroelectricity is distinct from that of magnetism, temperatures of ferroelectric and magnetic phase transition do not match with each other. As a result, the ME coupling coefficient, $\alpha = dP/dH$, is often rather small. However, in the type-II multiferroics, ferroelectricity is originated from the inversion symmetry breaking driven by spin order. As a result, the ME coupling in type-II multiferroics is generally higher than in type-I multiferroics because magnetic and electric orders, coining a single origin, develop at a nearly same temperature.

The emergence of P in type-II multiferroics has been established by the three well-known mechanisms, exchange striction,[8,9] inverse Dzyaloshinskii–Moriya interaction (or the spin current model),[5,10,11] and p–d hybridization.[6,12,13] The first two mechanisms can account for the emergence of spin-induced P when the material having large spin frustration exhibits the long wavelength spin textures of up–up–down–down or cycloidal spin orders, respectively. For example, TbMn$_2$O$_5$ exhibits P attributed to exchange striction between the Mn^{4+}—Mn^{3+} spin chains at 37 K and α is estimated to be 600 ps m^{-1}.[14] Furthermore, a Y-type hexaferrite Ba$_{0.5}$Sr$_{1.5}$Zn$_2$(Fe$_{0.92}$Al$_{0.08}$)$_{12}$O$_{22}$ with a transverse conical structure shows a giant ME coupling with α = 20 000 ps m^{-1} at 10 K,[10,11] while a Z-type hexaferrite Ba$_{0.48}$Sr$_{2.52}$Co$_2$Fe$_{24}$O$_{41}$ also has a strong ME coupling of $\alpha \approx$ 3000 ps m^{-1} even at room temperature.[15,16]

In the p–d hybridization mechanism, local electric dipole is generated from the spin-dependent electronic hybridization between p-orbital of a ligand ion and d-orbital of a transition

**ADVANCED
SCIENCE NEWS**
www.advancedsciencenews.com

**ADVANCED
ELECTRONIC
MATERIALS**
www.advelectronicmat.de

metal ion, which depends on spin direction of magnetic ion due to spin–orbit coupling. $Ba_2CoGe_2O_7$ and $CuFeO_2$ are known to develop P due to hybridization between O^{2-} ions and transition metal ions (Co^{2+} or Fe^{3+}).[6,13,17,18] As the non-centrosymmetric position of the magnetic ions is a prerequisite for this mechanism, P modulation and ME coupling can be in principle expected to occur in a single bonding between a magnetic ion and a ligand ion. Therefore, this mechanism, valid essentially in a single-spin limit, allows observation of ME coupling in a much shorter length scale than the other two mechanisms, which require interactions of at least two spins.

Recently, the interest in the 2D materials has been growing due to their potential in device applications and scientific novelties.[19–22] Given the successful observation of single ferroic order in a 2D system,[19,20] many van der Waals (vdW) materials have been theoretically predicted to become 2D multiferroics.[21,22] However, most of the studies have so far focused on the 2D multiferroics of type-I. For example, Lai et al.[23] have claimed that a $CuCrP_2S_6$ nanosheet shows multiferroic property at room temperature; they attribute P along the c-direction due to the non-centrosymmetric position of Cu^{1+} ions, indicating that the observed phenomenon belongs to the type-I class.

On the other hand, observation of the type-II multiferroicity and related large ME coupling have been limitedly known in 2D vdW compounds. For example, layered 2D magnets MI_2 (M = Ni and Co) have been known to exhibit bulk P due to a cycloidal spin ordering. Moreover, recent two studies on a very thin NiI_2 layers report rather inconsistent results of observing P in a single-layer and a bilayer limit, respectively; the lowest thickness limit for having finite P induced by the cycloidal spin order thus remains unresolved.[24,25] Moreover, broken inversion symmetry has been suggested in $MnPS_3$ below the Néel temperature (T_N) from the second harmonic generation study,[26] while the ME coupling has not been directly measured yet. Therefore, to realize large ME coupling in atomically thin 2D vdW compounds, it is necessary to find more examples of the type-II multiferroics of various origins. Furthermore, understanding on the origin of ME coupling is expected to elucidate a path to find the new type-II vdW compounds.

In this work, we present observation of strong ME coupling and magnetic field (H)-induced P modulation below T_N in a single crystal of $CuCrP_2S_6$, which can be understood by the symmetry analyses as originating from the p–d hybridization mechanism. With comprehensive measurements of magnetic and electric properties, the ME phase diagram is constructed in a bulk form. Our results further point to an interesting possibility of observing ME coupling in a single layer or in a single unit cell limit.
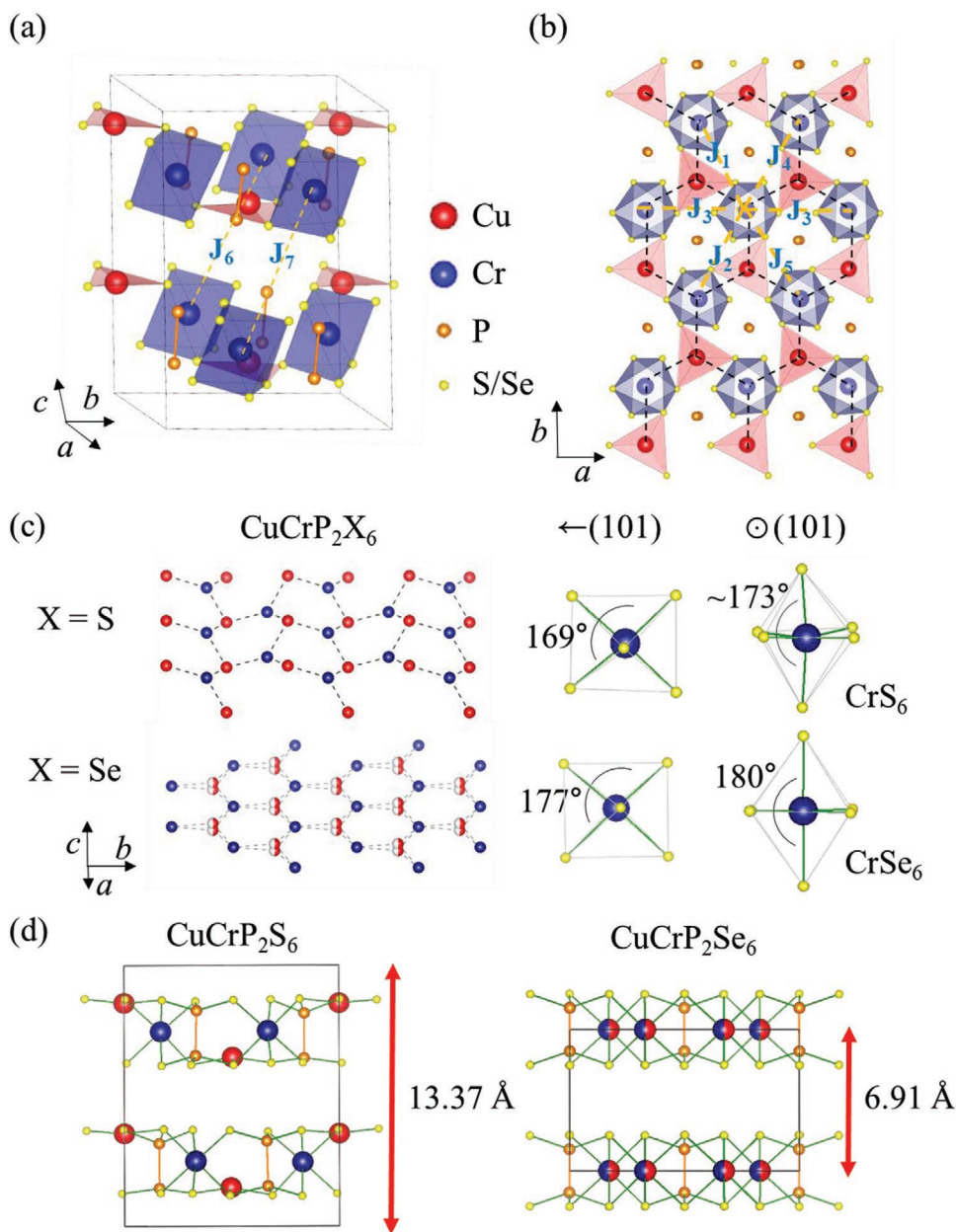
2. Experiments Results and Discussions

2.1. Experimental Results

$CuCrP_2S_6$ is a vdW magnet having stacked 2D layers connected by the vdW interaction (**Figure 1**a). Within each layer, Cu^{1+}, Cr^{3+} ions, and $P^{4+}-P^{4+}$ pairs, each of which sits in a hole made of a sulfur octahedron, form a triangular network; when only Cu^{1+} and Cr^{3+} ions are considered, they form a honeycomb

lattice in an ordered way, as depicted in Figure 1b. Here, only Cr^{3+} (d^3) is a magnetic ion that can contribute to a long range spin ordering because Cu^{1+} (or $P^{4+}-P^{4+}$) ions do not have a net spin moment with nominal d^{10} (or $3s^2$) electronic configuration.[27] Below 150 K, $CuCrP_2S_6$ undergoes an interesting structural phase transition to an antipolar structure described by the Pc space group, in which significant off-centering within the CuS_6 octahedra, forming nearly CuS_3 triangles in a single layer, results in an alternating c-axis positions of Cu^I (d^{10}) ions to exhibit antiparallel electric dipole arrangement. Figure 1a indeed displays such a crystal structure of $CuCrP_2S_6$ below 150 K, in which Cu atoms in the center of sulfuric triangles alternatively move up or down along the c^*-axis to form alternating electric dipoles, thereby resulting in a nearly antiferroelectric CuS_3 network.[28–30] Such a phase transition from room temperature $C2/c$ structure to the low temperature Pc phase should generally induce improper ferroelectricity, connected with appearance of small improper polarization in the ac-plane, if alternating electric dipoles from the off-centered Cu^+ ions do not completely cancel each other.

Related to this antipolar structure, the honeycomb lattice formed by the ordered Cu−Cr network becomes distorted, giving rise to shifts of Cr position from the center of each CrS_6 octahedron; Figure 1c presents the structure including only the Cu and Cr atoms, showing an evidence of a buckled honeycomb lattice. In contrast to the case of $CuCrP_2S_6$, $CuCrP_2Se_6$ has Cu atoms disordered among the two stable positions in the centers of sulfuric triangles so that the honeycomb lattice and the $CrSe_6$ octahedra are less distorted.[31,32] On the other hand, Cr ions inside the $CrSe_6$ octahedra are still located in the non-centrosymmetric position. However, it should be noted that in $CuCrP_2Se_6$, neighboring layers are coupled by translation, while each layer in $CuCrP_2S_6$ is stacked by this translation combined with a mirror operation across the ac-plane. As a result, the c lattice parameter (≈13.37 Å) in $CuCrP_2S_6$ is doubled as compared to that of $CuCrP_2Se_6$ (≈6.91 Å). The structural difference between the two compounds turns out to be essential for understanding the origin of ME coupling in $CuCrP_2S_6$ (vide infra).

According to the previous neutron diffraction study,[29] $CuCrP_2S_6$ is known to show a long-range antiferromagnetic (AFM) transition at $T_N = 32$ K. **Figure 2**b displays the magnetization M curves as a function of temperature (T) along the a-, b-, and c^*-directions (the c^*-direction is defined as the direction parallel to $a \times b$). At every direction, M versus T curve shows a clear anomaly at $T_N = 32$ K, being consistent with the AFM transition found in the neutron diffraction study.[29] Moreover, M/H along the b- and c^*-directions exhibit nearly T-independent M/H values, while along the a-direction, M/H does not start from the zero value at ≈2 K as conventional G-type AFM order shows, but from rather a low value of $\approx10^{-5}$. This behavior supports that the staggered moment of the AFM order in $CuCrP_2S_6$ is aligned nearly along the a-direction but with rather a weak uniaxial anisotropy. Previous magnetization[27] and neutron diffraction[29] studies pointed out that $CuCrP_2S_6$ indeed exhibits ferromagnetic (FM) order in the plane and the antiferromagnetic spin arrangement between the layers (A-type AFM order). These former results agree with our current M versus T results, supporting that the A-type AFM order is realized with a staggered moment aligned nearly along the a-axis. Upon high

**ADVANCED
SCIENCE NEWS**

www.advancedsciencenews.com

**ADVANCED
ELECTRONIC
MATERIALS**

www.advelectronicmat.de

Figure 1. a) Crystal structure of $CuCrP_2S_6$ below 150 K with the Pc space group, displaying six CrS_6 octahedra (blue), six CuS_3 triangles (red), and pairs of P^{4+} ions (orange) in a unit cell. b) The crystal structure projected onto the ab-plane, showing a honeycomb network (black dashed line) of CrS_6 octahedra and CuS_3 triangles (red). The exchange interaction paths (orange dashed lines) are also shown in (a) and (b). c) Comparison between the $CuCrP_2S_6$ and $CuCrP_2Se_6$ structures, displaying only Cu and Cr atoms and their nearest connection (gray dashed lines); in $CuCrP_2S_6$, the honeycomb lattice is buckled. White and red mixed balls indicate the disordered distribution of Cu atoms at two different positions. In both compounds, each Cr ion is off-centered inside one octahedron. d) The c-axis stacking of $CuCrP_2X_6$ (X = S and Se); each layer in $CuCrP_2Se_6$ is stacked by a translation along the c-axis, while each layer in $CuCrP_2S_6$ is stacked by this translation combined with a mirror operation across the ac-plane.

magnetic fields being applied along the ab-plane, the temperature where the anomaly emerges in the M versus T curve is reduced and finally disappears above 6 T (Figure S1, Supporting Information). This indicates that the AFM order is suppressed at high magnetic fields above 6 T and the system shows a forced ferromagnetic alignment at low temperatures, while it shows a crossover to the paramagnetic state at higher temperatures with increased thermal fluctuation.

Figure 2c,d depicts the M–H curves along the a-, b-, and c^*-directions at 10 K in a wide (−9 to 9 T) and a small (−0.9 to 0.9 T) H range, respectively. The M–H curve along the a-direction shows a slight curvature change at 0.3 T, whereas those along the b- and c^*-directions show linearly increasing behavior. The curvature change represents a spin-flop (SF) transition, which only happens along the a-direction at a low H of ≈0.3 T.[14] These observations in the M–H curves again support stabilization of
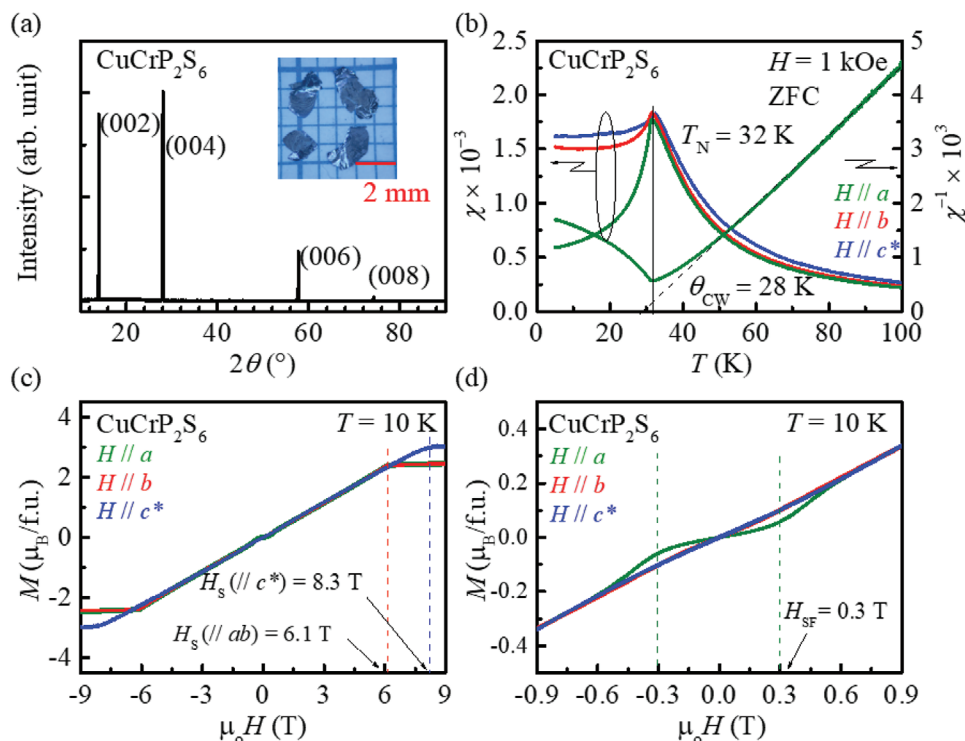
Figure 2. a) X-ray diffraction data, exhibiting reflection from the (0 0 2n) planes. The inset picture shows the ab facet of CuCrP$_2$S$_6$ single crystals. b) (Left) M/H versus T curve measured at $H = 1$ kOe in a warming process along the a- (green), b- (red), and c^*- (blue) axes after zero field cooling process (ZFC). Here, c^* equals $a \times b$. The right axis shows the $(M/H)^{-1}$ curve plotted to perform the Curie–Weiss fitting (dotted line). T_N and θ_{CW} refer to the Néel temperature and the Curie–Weiss temperature, respectively. c) M versus H curves along the a-, b-, and c^*-axes for $-9 \text{ T} < \mu_0H < 9$ T. The H_S is defined as the magnetic field at which the M–H curve is saturated. d) The M–H curves plotted at a low H-region, $-0.9 \text{ T} < \mu_0H < 0.9$ T. The slope change at 0.3 T represents the spin-flop (SF) transition that occurs only along the a-axis.

A-type AFM order with weak easy-axis anisotropy along the a-axis. When μ_0H is applied in the ab-plane (along the c^*-axis), the M is saturated at the saturation field $\mu_0H_S = 6.1$ T (8.3 T), in agreement with the forced FM alignment. The saturation magnetization M_s is 2.4 μ_B f.u.$^{-1}$ for $H//ab$ configuration, which is lower than the saturation moment expected from Cr^{3+} ions (3.00 μ_B).

We have confirmed the expected AFM ordering pattern by the Monte-Carlo simulations using the exchange constants obtained by density functional theory (DFT) calculation. **Table 1** summarizes the exchange interactions (J_n) marked in Figure 1a,b. The DFT calculation estimates the intralayer coupling to be FM and interlayer coupling to be effectively AFM, consistent with previous studies[27,29] and our present experimental data. Figure 2b shows a long-range AFM ordering of bulk samples while the Curie–Weiss temperature (θ_{CW}) is positive +28 K, demonstrating dominant FM interaction. Putting all the information together, it is inferred that spins align

along the a-direction forming a FM arrangement in the ab-plane and an AFM alignment between the planes along the c^*-direction.

Figure 3a compares the three curves measured at 5 K with the application of $H//ab$-plane; magnetoelectric current (I_{ME}) (top) and P_{c^*} variation (middle) along the c^*-direction (ΔP_{c^*}) measured at a positive (or negative) electric field bias $+E_{c^*} = 5$ kV cm^{-1} (or $-E_{c^*}$) applied along the c^*-axis, and finally dielectric constant (ε_{c^*}). Here, ΔP_{c^*} represents H-induced P_{c^*} modulation with a reference to the value at the starting field, i.e., either 9 or -9 T. The four kinds of I_{ME} curves exhibit a peak (or a dip) structure at $\pm\mu_0H_S = 6.1$ T for $+E_{c^*}$ (or $-E_{c^*}$) and smooth variations between $-H_S$ and H_S; the sign of I_{ME} is reversed when E_{c^*} changes its sign. Hence, ΔP_{c^*}, obtained from the integration of I_{ME}, nearly changes its sign when the direction of the electric field bias is reversed at a field region of $-H_S \leq H \leq H_S$, termed here as ME phase. Consistent with this, $\varepsilon_{c^*}(H)$ curves exhibit a peak at both $+H_S$ and $-H_S$, indicating that at the saturation field of spin moment, existing antiferroelectric (or improper ferroelectric) domains, and related ME properties are significantly modified at the phase boundaries between the AFM and ME phases and the paramagnetic (PM) and antiferroelectric (AFE) phases. On the other hand, the modulation of P_{c^*} was not found for the field applied out-of-plane, i.e., for $H//c^*$ (Figure S2, Supporting Information).[33]

We have subsequently performed the same I_{ME} measurements for $H//ab$ at various temperatures from 5 to 40 K and

Table 1. Exchange constants J_i ($i = 1$–7) of CuCrP$_2$S$_6$ estimated from the DFT calculations. J_1–J_5 indicate the intralayer exchange constants and J_6, J_7 are the interlayer exchange constants, as depicted in Figure 1a,b.

	J_1	J_2	J_3	J_4	J_5	J_6	J_7
Cr−Cr distance [Å]	5.832	5.868	5.935	6.008	6.044	6.674	6.718
Intralayer coupling [meV]	−3.66	−2.8	−1.9	−2.66	−1.62	0.2	−0.096
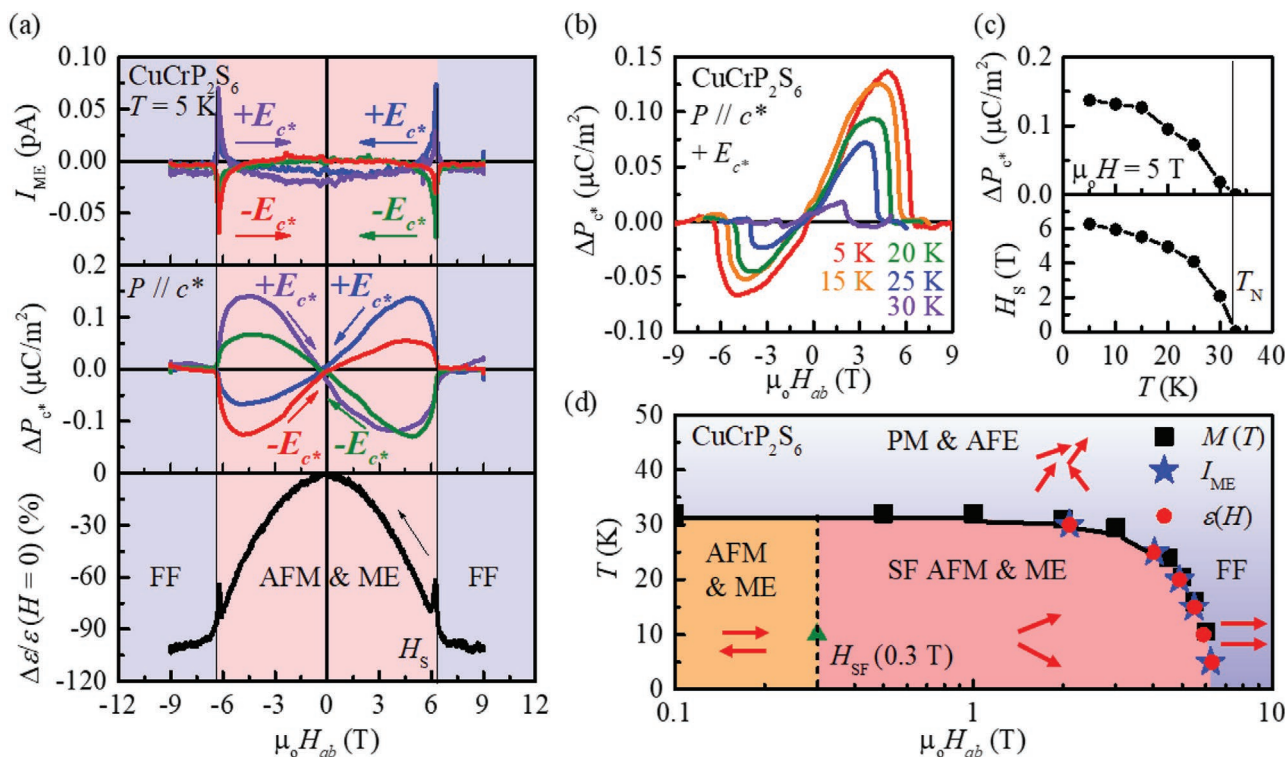
Figure 3. a) Magnetoelectric current I_{ME} (top), variation of P along the $c*$-axis ΔP_{c*} (middle), and the $c*$-axis dielectric constant ε_{c*} (bottom) measured at 5 K for $H//ab$. ΔP_{c*} was calculated by integrating the ME current with time, which is measured under an electric field bias $E_{c*} = 5$ kV cm^{-1}. b) ΔP_{c*} (H) curves at various temperatures from 5 to 33 K. c) ΔP_{c*} values selected at $H = 5$ T and H_S below T_N, strongly supporting that ΔP_{c*} emerges, coined to the long range AFM order. d) Electrical and magnetic phase diagram of CuCrP$_2$S$_6$ for $H//ab$. The circles, stars, and squares represent the anomalies found in ε_{c*}, I_{ME}, and $M(T)$ curves, respectively. The red arrows denote the direction of spins on each layer in a single unit cell at each phase. Here, the acronyms AFM, PM, AFE, ME, and FF refer to antiferromagnetic, paramagnetic, antiferroelectric, magnetoelectric, and forced ferromagnetic states, respectively.

the resultant ΔP_{c*} are displayed in Figure 3b. The magnitude of ΔP_{c*} is gradually decreasing and the H_S where ΔP_{c*} shows a sudden increase is systematically suppressed upon heating. Figure 3c summarizes the results. Both ΔP_{c*} and H_S are suppressed at $T_N = 32$ K, demonstrating the presence of large ME effect below T_N. For above T_N, although the crystal space group allows, in principle, electric polarization in the ac-plane, P_{c*} modulation with H has not been found.

Based on these experimental results, we have determined magnetic and electrical phase diagram of CuCrP$_2$S$_6$ for $H//ab$, as presented in Figure 3c. There exist three distinct phases. First, a PM and AFE (or improper ferroelectric) phase, resulting from the regular ordering of off-centered Cu^{1+} ions is stabilized above $T_N = 32$ K and below 150 K. Therefore, the AFE phase (or improper FE phase) seems to be stabilized above T_N, being consistent with the previous studies.[23,28] Below 32 K and at fields lower than 0.3 T, the A-type AFM state, of which staggered moment is nearly parallel to the a-axis, is stabilized. However, the application of external H along the a-axis induces the SF transition at $H_{SF} = 0.3$ T to result in the spin-flopped AFM and ME states, in which the staggered moment becomes perpendicular to the a-axis, as pictorially described in the evolution of two arrows inside Figure 3c. In this phase, the out-of-plane polarization, i.e., P_{c*} can be significantly modulated by external $H//ab$. The P_{c*} modulation with H nearly disappears at high H when the

spins are fully aligned along the a-axis to reach a forced ferromagnetic (FF) state at low temperatures. Although there might still exist a secondary ME effect at the FF state such as the magnetostriction-induced one, we neglect here such small ME effects. With the increased thermal fluctuation, the system is then smoothly connected to the PM and AFE phases at high temperatures. We expect that the antipolar structure derived from the displacements of Cu^{1+} ions should still survive in the AFE region even at high magnetic fields. Further studies are needed to identify the exact magnetic and electric structures of those high field or high temperature phases.

2.2. Symmetry Analysis and Discussions

CuCrP$_2$S$_6$ has a crystal structure described by the space group Pc, which has two symmetry elements: $E = (x, y, z)$ and $\sigma_y = (x, -y, z + 0.5)$. The unit cell contains two inequivalent Cr atomic positions, each of which is composed of two Cr atoms. The Cr atoms can be labeled Cr$_{ij}$ and their atomic coordinates are

$$Cr_{11} = (0, 0.332, 0.25), Cr_{12} = (0, 0.668, 0.75),$$
$$Cr_{21} = (0.527, 0.830, 0.246), Cr_{22} = (0.527, 0.170, 0.746) \quad (1)$$

Therefore, Cr$_{11}$ and Cr$_{12}$ comprise one inequivalent set of atoms, whereas Cr$_{21}$ and Cr$_{22}$ constitute another set.

Table 2. Transformation properties of order parameters by group elements of Pc space group.

Irreducible representation	E	σ_y	OPs
Γ_1	+1	+1	M_{1b}, M_{2b}, A_{1a}, A_{1c*}, A_{2a}, A_{2c*}, P_a, P_{c*}
Γ_2	+1	−1	M_{1a}, M_{1c*}, M_{2a}, M_{2c*}, A_{1b}, A_{2b}, P_b

The FM and AFM order parameters (OPs) can be defined as the sum and difference of the Cr spins, respectively

$$
\begin{aligned}
\vec{M}_1 &= \vec{S}_{11} + \vec{S}_{12} \\
\vec{M}_2 &= \vec{S}_{21} + \vec{S}_{22} \\
\vec{A}_1 &= \vec{S}_{11} - \vec{S}_{12} \\
\vec{A}_2 &= \vec{S}_{21} - \vec{S}_{22}
\end{aligned}
\tag{2}
$$

Here, $\vec{M}$ indicates the FM OPs and $\vec{A}$ is AFM OPs, whereas $\vec{S}_{ij}$ indicates the spins of Cr$_{ij}$. The OPs are transformed by the symmetry elements of Pc space group, which have +1 or −1 matrices depending on the transformational properties of OPs, as summarized in **Table 2**. Our main concerns are FM and AFM OPs within the ab-plane and P_{c*}, because we experimentally applied H in the ab-plane and E along the $c*$-direction. In the following text, since $\vec{A}_1$ and $\vec{A}_2$ have the same transformational properties (as well as $\vec{M}_1$ and $\vec{M}_2$), we can omit the subscript for simplicity and consider the OPs $\vec{M}$ and $\vec{A}$. Therefore, the thermodynamic potential, Φ, which should be invariant under the symmetry operations, can be written as

$$
\begin{aligned}
\Phi = {} & \frac{\alpha_1}{2} A_a^2 + \frac{\alpha_2}{2} A_b^2 + \frac{\beta_1}{2} A_a^4 + \frac{\beta_2}{2} A_b^4 + \frac{1}{2\chi_a} M_a^2 + \frac{1}{2\chi_b} M_b^2 - \\
& M_a H_a - M_b H_b + \frac{a_1}{2} P_{c*}^2 + a_2 M_a A_b P_{c*} + a_3 M_b A_a P_{c*}
\end{aligned}
\tag{3}
$$

where α_1, α_2, β_1, β_2, a_1, a_2, and a_3 are the phenomenological coefficients, and χ_a and χ_b are the magnetic susceptibilities along the axes a and b, respectively. Minimization of Φ with respect to P_{c*} yields

$$
P_{c*} = \frac{1}{a_1}\left(a_2 M_a A_b + a_3 M_b A_a \right)
\tag{4}
$$

Thus, P_{c*} is expressed by the coupled terms between the perpendicular components of $\vec{M}$ and $\vec{A}$ in the ab-plane. Therefore, CuCrP$_2$S$_6$ is a linear ME in the AFM phase when $\vec{A} \neq 0$ because of the linear coupling between magnetic field and polarization. Assuming that the AFM ordering occurs in the ab-plane and that the AFM vector easily aligns perpendicular to the applied magnetic field since the spin-flop field $H_{SF} \approx 0.3$ T is rather small, one can find that $P_{c*} \propto H(H_S^2 - H^2)^{1/2}$, where H is the magnetic field in the ab-plane. Here, we assume that increasing magnetic field gradually aligns the spins along the field, resulting in decrease of the AFM order parameter, which can be described by the relation $M^2 + A^2 = $ const. **Figure 4**a depicts the comparison between experimental data and the equation derived from the symmetry and thermodynamic analyses, resulting in the successful theoretical explanation of the experimental results. It is noted in Figure 4a that experimental data
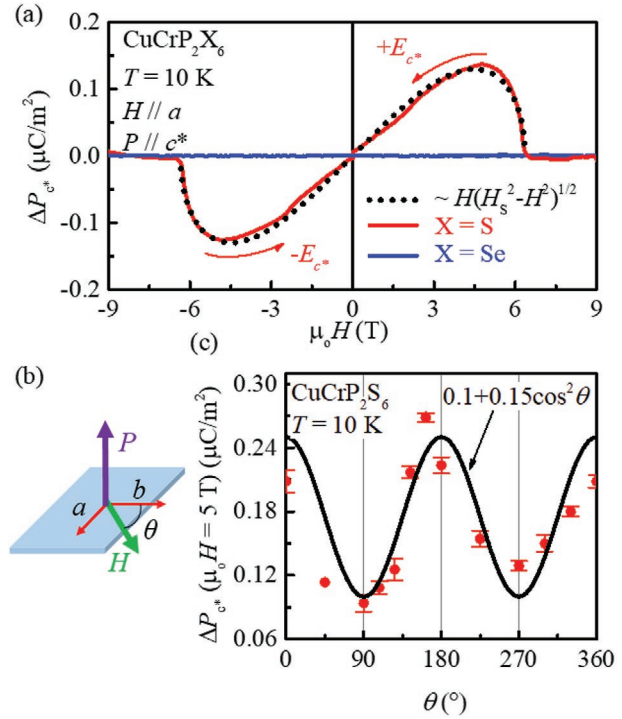
Figure 4. a) Electric polarization of CuCrP$_2$S$_6$ (red solid line) and CuCrP$_2$Se$_6$ (blue solid line) along the $c*$-direction at 5 K for $H//a$. The black dotted line represents the curve fitting results with a functional form of $\sim H(H_S^2 - H^2)^{1/2}$. To rule out the effect of competing domain switching by the electric field bias, the experimental $\Delta P_{c*}(H)$ curves are plotted based on the two data sets, one obtained from $H = 9$–0 T for $+E_{c*}$ and the other from $H = -9$ to 0 T for $-E_{c*}$, as represented by the two red solid arrows. b) The experimental configuration for the measurement of ΔP_{c*} in a rotating, in-plane H. θ is determined as the rotation angle from the b-axis. c) The ΔP_{c*} values at $H = 5$ T and $T = 10$ K as a function of θ (red solid circles) and a fitted curve based on a functional form of $(0.1 + 0.15\cos^2\theta)$ (black solid line).

of ΔP_{c*} measured under $+E_{c*}$ and $-E_{c*}$ are plotted in the positive and negative H regions, respectively, because a preferential ferroelectric polarization induced in a positive H region by $+E_{c*}$ can be reduced by the domain competition once H changes its sign.

Figure S3 (Supporting Information) exhibits $(|\Delta P_{pos}| - |\Delta P_{neg}|)$ values depending on the sign of E-bias, where $|\Delta P_{pos}|$ and $|\Delta P_{neg}|$ are defined as the absolute values of positive and negative ΔP extrema, respectively, which are estimated in the four curves of ΔP–H in Figure 3a.[33] It is observed that $|\Delta P_{pos}| - |\Delta P_{neg}|$ is always positive (negative) when positive (negative) E-bias is applied regardless of the initial starting H-value, i.e., either +9 or −9 T. This is because positive (negative) P domains created by $+E_{c*}$ ($-E_{c*}$) bias in Figure 3a always reduces its absolute value due to creation of competing P domains of opposite direction with the H sign change. This observation is also consistent with the above symmetry analyses showing the linear coupling between the generated P_c and M_a (thus H_{ab}). Here, we rule out such domain competition effect and purely consider the crystal symmetry for the analysis.

We have also performed ΔP_{c*} measurements with variation of azimuthal angle θ for which the in-plane H rotates in the

**ADVANCED
SCIENCE NEWS**

www.advancedsciencenews.com

**ADVANCED
ELECTRONIC
MATERIALS**

www.advelectronicmat.de

AFM phase. Figure 4b displays the experimental configuration; $\overline{H}$ is applied and rotated within the ab-plane and θ is defined as the angle between $\overline{H}$ and the b-axis. In this case, $\overline{M}$ is parallel to $\overline{H}$, while $\overline{A}$ is perpendicular to $\overline{H}$, giving rise to the relation, $(M_a, M_b) = (\sin\theta, \cos\theta)$ and $(A_a, A_b) = (-\cos\theta, \sin\theta)$. As a result, P_{c*} can be found as

$$P_{c*} = \frac{1}{a_1}\left(a_2\sin^2\theta - a_3\cos^2\theta\right) = p_1 + p_2\cos^2\theta \tag{5}$$

where p_1 and p_2 are constants. Figure 4c shows the comparison with the experimental data, where the p_1 and p_2 values are estimated to be 0.10 and 0.15, respectively. A slight deviation of the theoretical curve from the experimental data is likely due to the higher order ME interaction terms present in the thermodynamic potential or caused by a slight misalignment of the sample.

In the type-II multiferroic materials, the microscopic origin of ME coupling is usually ascribed to three types: exchange striction,[4,8] inverse Dzyaloshinskii–Moriya (DM) interaction or the spin current model,[5,10,11] and p–d hybridization.[6,12,13,17] In the exchange striction mechanism, P is generated by the symmetric exchange interaction between the neighboring magnetic ions; rare-earth orthorhombic manganites $RMnO_3$ (R = Ho–Lu) with E-type AFM order,[8,9] the Mn^{3+}–Mn^{4+} mixed manganites RMn_2O_5,[34] and Ca_3CoMnO_6 with spin $\uparrow\uparrow\downarrow\downarrow$ ordering[35] are widely known examples. In $CuCrP_2S_6$, the spins of Cr^{3+} ions show FM alignment within the ab-planes and AFM stacking of planes along the $c*$-direction. The ME interactions responsible for the appearance of P_{c*} have thus the forms

$$P_{c*}M_{ia}A_{jb} \text{ or } P_{c*}M_{ib}A_{ja} \left(i, j = 1, 2\right) \tag{6}$$

Expressing these interactions in terms of spins of Cr atoms shows that there are no symmetric exchange interactions, which precludes the exchange striction mechanism in $CuCrP_2S_6$.

In turn, the inverse DM mechanism[5] arises from the antisymmetric spin interaction. Such ME coupling is only applicable in the case of noncollinear spin structures, to which also belong spatially modulated magnetic orderings, such as, e.g., cycloidal or transverse conical spin structures. Previous neutron diffraction studies of $CuCrP_2S_6$ show no evidence of a canted spin structure. In fact, any component of the $\overline{A}$ can induce components of $\overline{M}$ (Table 2), resulting in the appearance of weak ferromagnetism that is not confirmed experimentally. The magnetic ground state of $CuCrP_2S_6$ is characterized by ferromagnetic alignment of spins within each vdW layer and stacking of each layer along the $c*$-direction with antiferromagnetic spin alignment (A-type AFM order). Upon external magnetic field being applied, the spins start to being aligned along the field, which leads to canting of total magnetization of layers with respect to neighboring layers so that additional electric polarization can be induced. Therefore, the appearance of additional H-induced polarization can in principle be ascribed to inverse DM-like interaction. However, due to rather large distance between the spins in neighboring layers (>6.67 Å), which are separated by the vdW gap, one can arguably exclude this mechanism.

2.3. Comparison with the Case of $CuCrP_2Se_6$

The promising mechanism of ME coupling is thus p–d hybridization, in which local electric dipole is generated from the electronic hybridization between p-orbital of a ligand ion and d-orbital of a transition metal magnetic ion. The electronic hybridization depends on spin direction of magnetic ion due to spin–orbit coupling and in the most simplified form, local electric polarization can be written as

$$P_{il}^{pd} \propto e_{il}\left(S_i \cdot e_{il}\right)^2 \tag{7}$$

where e_{il} is parallel to the bonding direction connecting the magnetic ion i and ligand ion l. For example, the origin of ME coupling in $CuFeO_2$ with incommensurate spiral spin ordering has been ascribed to the spin-direction-dependent hybridization between d-orbital of Fe^{3+} ions and p-orbital of O^{2-} ions.[18] $Ba_2CoGe_2O_7$ also has H-induced P originating from p–d hybridization.[13,17] The requirement for the validity of such a single-ion microscopic mechanism for the ME coupling is the non-centrosymmetric position of the magnetic ions, which is the case in the polar structure of $CuCrP_2S_6$. In fact, from the above ME interactions, one can deduce the single-ion contributions to the ME effect

$$\begin{aligned} P_{c*}\left(S_{11a}S_{11b} - S_{12a}S_{12b}\right) \\ P_{c*}\left(S_{21a}S_{21b} - S_{22a}S_{22b}\right) \end{aligned} \tag{8}$$

To investigate whether the structural difference summarized in Figure 1 affects to ME coupling in this system, we have grown $CuCrP_2Se_6$ single crystal, as a counterpart compound of $CuCrP_2S_6$, and conducted the similar measurements. As mentioned in the previous session for the crystal structure, the distortion of honeycomb network is much more relieved in $CuCrP_2Se_6$ than in $CuCrP_2S_6$. The crystal structure of $CuCrP_2Se_6$ is also polar similar to $CuCrP_2S_6$, but belongs to the space group $C2$. This means that like the case of $CuCrP_2S_6$, the local symmetry of Cr atoms in $CuCrP_2Se_6$ is non-centrosymmetric and polar, which allows the single-ion contributions to the ME properties albeit being arguably smaller than in $CuCrP_2S_6$, because the $CrSe_6$ octahedra in $CuCrP_2Se_6$ are much less distorted (Figure 1c).

Figure S4 (Supporting Information) verifies that $CuCrP_2Se_6$ undergoes an AFM transition at 42 K and field-induced saturation at 5.5 T at 5 K, similar to the behavior in $CuCrP_2S_6$.[33] Surprisingly, the H-induced P is not observed in $CuCrP_2Se_6$ (Figure 4a). The absence of ME properties in $CuCrP_2Se_6$ can be understood as follows. The neutron diffraction studies reveal that the magnetic structure of $CuCrP_2Se_6$ below T_N is similar to that of $CuCrP_2S_6$, i.e., ferromagnetic vdW layers that are stacked along the $c*$-direction with the AFM alignment, resulting in the A-type antiferromagnetic order.[31] However, as explained in Figure 1c, in $CuCrP_2Se_6$, neighboring layers are only coupled by translation so that the unit cell along the c-axis is not doubled as in the case of $CuCrP_2S_6$. Therefore, the A-type AFM spin order between the two vdW layers in $CuCrP_2Se_6$ results in a magnetic structure that is described by the nonzero wavevector (0, 0, 1/2), leading to multiplication of the unit cell. This unit cell doubling due to the A-type AFM order thereby

**ADVANCED
SCIENCE NEWS**
www.advancedsciencenews.com

**ADVANCED
ELECTRONIC
MATERIALS**
www.advelectronicmat.de

leads to cancellation of net polarization generated by the p–d hybridization mechanism in each layer and thus precludes the ME interactions in $CuCrP_2Se_6$.

Our comparative studies in both $CuCrP_2S_6$ and $CuCrP_2Se_6$, having similar magnetic orderings and off-centered Cr^{3+}, provide the solid understanding that the origin of H-induced P in this class of materials is the p–d hybridization mechanism coming from the off-centered Cr^{3+} octahedral sites. This allows in principle the observation of type II multiferroic behavior in both compounds in a single layer limit regardless of the spin ordering pattern. However, in bulk materials, the crystal symmetry, i.e., the way the layers are stacked is also important to observe the net polarization. The net polarization cancels out due to the crystal symmetry creating the unit cell doubling by the spin order in $CuCrP_2Se_6$, while it does not in $CuCrP_2S_6$. Our understanding further predicts that the net polarization might survive in the thin layers with the odd number of the c-axis unit cells in $CuCrP_2Se_6$, while it can survive in every stacked vdW layers down to a single layer limit in $CuCrP_2S_6$.

3. Conclusion

In conclusion, we have newly discovered a magnetic-field-induced ferroelectricity and associated ME effects below its Néel temperature 32 K in a vdW antiferromagnet $CuCrP_2S_6$ and identified the spin-dependent p–d hybridization mechanism arising from the off-centered Cr^{3+} cations located inside the sulfur octahedra as the main origin of the ME effect. Experimental investigations of magnetic/electrical properties and DFT calculations demonstrate that the bulk sample exhibits an A-type AFM ordering with weak anisotropy along the a-direction. Within the AFM phase, $CuCrP_2S_6$ shows the large linear ME effect. Moreover, in this AFM phase, P is controlled by magnetic field and eventually suppressed at the saturation field of M where the spin-flopped AFM phase disappears with the forced ferromagnetic alignment. The symmetry analysis based on the Pc space group and the azimuthal angle dependence of ΔP successfully explains the ΔP–H curve behavior by the p–d hybridization mechanism. Because the p–d hybridization mechanism allows the generation of a local electric dipole nearby a magnetic ion, we envision that our understanding on the mechanism can be further useful to find numerous 2D vdW multiferroic materials down to a single layer limit.

4. Experimental Section

Single Crystal Growth: $CuCrP_2S_6$ single crystals were grown by the chemical vapor transport method with sulfur as a self-transport agent. The stoichiometric Cu, Cr, P, and S powder of high purity was mixed as a starting material and sealed in an evacuated quartz tube, which was located in well-calibrated tube furnace with a temperature gradient from 650 to 600 °C for 2 weeks. The growth condition of $CuCrP_2Se_6$ was almost similar, except that $SeCl_4$ was used as a transport agent. The single crystals of thin plate shape with the sizes of $\approx 2 \times 2 \times 0.5$ mm³ were grown in the cold zone (the inset of Figure 2a).

Structural and Transport Properties: The structural analysis was performed by high-resolution X-ray diffractometer (Empyrean, PANalytical). For the dielectric constant and I_{ME} measurements along the $c*$-direction, the sample was cut into parallel plate shape and two copper wires were attached on the ab-planes of the sample by covering

it with a silver paste, DuPont 4929N. The sample was mounted on the lab-made multifunctional probe and connected to a pair of micro-coaxial wire. Dielectric constant and I_{ME} were measured by a capacitance bridge (Andeen-Hagerling 2550A) and an electrometer (Keithley 617), respectively. To measure I_{ME}, two schemes, i.e., electric-field-biased and poled measurements, were employed. In the former, I_{ME} was recorded under the external E applied by an in-built DC voltage source. For the poled case, $E = 5$ kV cm^{-1} was applied along the $c*$-axis in a high field state ($\mu_0 H = 9$ T) and after H reached to a low-field, E was turned off and the two electrodes were shortened before starting the I_{ME} measurements to remove possible trapped charges during the E poling procedure. P modulation with H was estimated by integrating the I_{ME} by time. Temperature and magnetic field were varied using the Physical Property Measurement System (Quantum Design) during the measurements of dielectric constant and I_{ME}. Finally, a vibrating sample magnetometer was used to measure magnetization from 2 to 300 K.

DFT Calculations and Monte-Carlo Simulations: DFT calculations were performed using the Vienna Ab initio Simulation Package[36] using projected augmented wave method[37] within the generalized gradient approximation (GGA) corrected by means of the GGA+U formalism for the Cu and Cr ions with $U_{eff} = U - J = 5$ and 3 eV, respectively.[38] The van der Waals energy correction was calculated using the method of Grimme.[39] Brillouin zone integration was done using the Monkhorst–Pack scheme, the energy cutoff was set to 500 eV, whereas the crystal structure was relaxed until the forces on atoms were greater than 10^{-3} eV Å^{-1}. The exchange constants were determined performing collinear spin polarized calculations and fitting relative energies of different magnetic structures to the Hamiltonian.

Classical Monte-Carlo simulations employing the Metropolis scheme were performed using the exchange constants obtained from DFT calculations and the Hamiltonian

$$\mathcal{H} = \sum_{i \neq j} J_{ij} \bar{S}_j \cdot \bar{S}_j + \sum_i D_{i\alpha} S_{i\alpha}^2 \tag{9}$$

where classical unit spins $\bar{S}_j$ and the anisotropy constants $D_{i\alpha}$ were employed. The simulation box was chosen to be $14 \times 14 \times 14$ unit cells, the thermalization procedure at each temperature lasted for 10^4 Monte-Carlo steps per spins (MCS), whereas the subsequent 10^4 MCS were used for gathering statistics.

Supporting Information

Supporting Information is available from the Wiley Online Library or from the author.

Conflict of Interest

The authors declare no conflict of interest.

Data Availability Statement

The data that support the findings of this study are available from the corresponding author upon reasonable request.

[1] R. Ramesh, N. A. Spaldin, *Nat. Mater.* **2007**, *6*, 21.

[2] S.-W. Cheong, M. Mostovoy, *Nat. Mater.* **2007**, *6*, 13.

[3] Y. Tokura, S. Seki, N. Nagaosa, *Rep. Prog. Phys.* **2014**, *77*, 076501.

[4] T. Zhao, A. Scholl, F. Zavaliche, K. Lee, M. Barry, A. Doran, M. P. Cruz, Y. H. Chu, C. Ederer, N. A. Spaldin, R. R. Das, D. M. Kim, S. H. Baek, C. B. Eom, R. Ramesh, *Nat. Mater.* **2006**, *5*, 823.

[5] H. Katsura, N. Nagaosa, A. V. Balatsky, *Phys. Rev. Lett.* **2005**, *95*, 057205.

[6] C. Jia, S. Onoda, N. Nagaosa, J. H. Han, *Phys. Rev. B* **2006**, *74*, 224444.

[7] M. Fiebig, T. Lottermoser, D. Meier, M. Trassin, *Nat. Rev. Mater.* **2016**, *1*, 16046.

[8] I. A. Sergienko, C. Şen, E. Dagotto, *Phys. Rev. Lett.* **2006**, *97*, 227204.

[9] S. Picozzi, K. Yamauchi, B. Sanyal, I. A. Sergienko, E. Dagotto, *Phys. Rev. Lett.* **2007**, *99*, 227201.

[10] S. H. Chun, Y. S. Chai, Y. S. Oh, D. Jaiswal-Nagar, S. Y. Haa, I. Kim, B. Lee, D. H. Nam, K.-T. Ko, J. H. Park, J.-H. Chung, K. H. Kim, *Phys. Rev. Lett.* **2010**, *104*, 037204.

[11] Y. S. Chai, S. Kwon, S. H. Chun, I. Kim, B.-G. Jeon, K. H. Kim, S. Lee, *Nat. Commun.* **2014**, *5*, 4208.

[12] K. Yamauchi, P. Barone, S. Picozzi, *Phys. Rev. B* **2011**, *84*, 165137.

[13] J. W. Kim, S. Khim, S. H. Chun, Y. Jo, L. Balicas, H. T. Yi, S.-W. Cheong, N. Harrison, C. D. Batista, J. H. Han, K. H. Kim, *Nat. Commun.* **2014**, *5*, 4419.

[14] Y. S. Oh, B.-G. Jeon, S. Y. Haam, S. Park, V. F. Correa, A. H. Lacerda, S.-W. Cheong, G. S. Jeon, K. H. Kim, *Phys. Rev. B* **2011**, *83*, 060405(R).

[15] Y. Kitagawa, Y. Hiraoka, T. Honda, T. Ishikura, H. Nakamura, T. Kimura, *Nat. Mater.* **2010**, *9*, 797.

[16] S. H. Chun, Y. S. Chai, B.-G. Jeon, H. J. Kim, Y. S. Oh, I. Kim, H. Kim, B. J. Jeon, S. Y. Haam, J.-Y. Park, S. H. Lee, J.-H. Chung, J.-H. Park, K. H. Kim, *Phys. Rev. Lett.* **2012**, *108*, 177201.

[17] H. Murakawa, Y. Onose, S. Miyahara, N. Furukawa, Y. Tokura, *Phys. Rev. Lett.* **2010**, *105*, 137202.

[18] T. Arima, *J. Phys. Soc. Jpn.* **2007**, *76*, 073702.

[19] K. Chang, J. Liu, H. Lin, N. Wang, K. Zhao, A. Zhang, F. Jin, Y. Zhong, X. Hu, W. Duan, Q. Zhang, L. Fu, Q.-K. Xue, X. Chen, S.-H. Ji, *Science* **2016**, *353*, 274.

[20] C. Gong, L. Li, Z. Li, H. Ji, A. Stern, Y. Xia, T. Cao, W. Bao, C. Wang, Y. Wang, Z. Q. Qiu, R. J. Cava, S. G. Louie, J. Xia, X. Zhang, *Nature* **2017**, *546*, 265.

[21] J. Qi, H. Wang, X. Chen, X. Qian, *Appl. Phys. Lett.* **2018**, *113*, 043102.

[22] J. R. Reimers, S. A. Tawfik, M. J. Ford, *Chem. Sci.* **2018**, *9*, 7620.

[23] Y. Lai, Z. Song, Y. Wan, M. Xue, C. Wang, Y. Ye, L. Dai, Z. Zhang, W. Yang, H. Du, J. Yang, *Nanoscale* **2019**, *11*, 516.

[24] H. Ju, Y. Lee, K.-T. Kim, I. H. Choi, C. J. Roh, S. Son, P. Park, J. H. Kim, T. S. Jung, J. H. Kim, K. H. Kim, J.-G. Park, J. S. Lee, *Nano Lett.* **2021**, *21*, 5126.

[25] Q. Song, C. A. Occhialini, E. Ergecen, B. Ilyas, K. Watanabe, T. Taniguchi, N. Gedik, R. Comin, arXiv:2106.07661, v1, unpublished.

[26] H. Chu, C. J. Roh, J. O. Island, C. Li, S. Lee, J. Chen, J.-G. Park, A. F. Young, J. S. Lee, D. Hsieh, *Phys. Rev. Lett.* **2020**, *124*, 027601.

[27] P. Colombet, A. Leblanc, M. Danot, J. Rouxel, *J. Solid State Chem.* **1982**, *41*, 174.

[28] V. Maisonneuve, V. B. Cajipe, C. Payen, *Chem. Mater.* **1993**, *5*, 758.

[29] V. Maisonneuve, C. Payen, V. B. Cajipe, *J. Solid State Chem.* **1995**, *116*, 208.

[30] K. Moriya, N. Kariya, A. Inaba, T. Matsuo, I. Pritz, Y. M. Vysochanskii, *Solid State Commun.* **2005**, *136*, 173.

[31] X. Bourdon, V. Maisonneuve, V. B. Cajipe, C. Payen, J. E. Fischer, *J. Alloys Compd.* **1999**, *283*, 122.

[32] R. Pfeiff, R. Kniep, *J. Alloys Compd.* **1992**, *186*, 111.

[33] See the Supporting Information for full experimental details.

[34] H. Kimura, Y. Sakamoto, M. Fukunaga, H. Hiraka, Y. Noda, *Phys. Rev. B* **2013**, *87*, 104414.

[35] Y. J. Choi, H. T. Yi, S. Lee, Q. Huang, V. Kiryukhin, S.-W. Cheong, *Phys. Rev. Lett.* **2008**, *100*, 047601.

[36] G. Kresse, J. Furthmüller, *Phys. Rev. B* **1996**, *54*, 11169.

[37] P. E. Blöchl, *Phys. Rev. B* **1994**, *50*, 17953.

[38] S. L. Dudarev, G. A. Botton, S. Y. Savrasov, C. J. Humphreys, A. P. Sutton, *Phys. Rev. B* **1998**, *57*, 1505.

[39] S. Grimme, *J. Comput. Chem.* **2006**, *27*, 1787.

2101072 (9 of 9)